
ARE VISION xLSTM EMBEDDED UNET MORE RELIABLE IN MEDICAL 3D IMAGE SEGMENTATION?

Pallabi Dutta

Machine Intelligence Unit
Indian Statistical Institute, Kolkata 700108, India
duttapallabi_r@isical.ac.in

Soham Bose

Department of Computer Science and Engineering
Jadavpur University, Kolkata 700032, India
sohamb.cse.ug@jadavpuruniversity.in

Swalpa Kumar Roy

Department of Computer Science and Engineering
Alipurduar Government Engineering
and Management College, West Bengal 736206, India
swalpa@agenc.ac.in

Sushmita Mitra

Machine Intelligence Unit
Indian Statistical Institute, Kolkata 700108, India
sushmita@isical.ac.in

ABSTRACT

The advancement of developing efficient medical image segmentation has evolved from initial dependence on Convolutional Neural Networks (CNNs) to the present investigation of hybrid models that combine CNNs with Vision Transformers. Furthermore, there is an increasing focus on creating architectures that are both high-performing in medical image segmentation tasks and computationally efficient to be deployed on systems with limited resources. Although transformers have several advantages like capturing global dependencies in the input data, they face challenges such as high computational and memory complexity. This paper investigates the integration of CNNs and Vision Extended Long Short-Term Memory (Vision-xLSTM) models by introducing a novel approach called **UVixLSTM**. The Vision-xLSTM blocks captures temporal and global relationships within the patches extracted from the CNN feature maps. The convolutional feature reconstruction path upsamples the output volume from the Vision-xLSTM blocks to produce the segmentation output. Our primary objective is to propose that Vision-xLSTM forms a reliable backbone for medical image segmentation tasks, offering excellent segmentation performance and reduced computational complexity. *UVixLSTM* exhibits superior performance compared to state-of-the-art networks on the publicly-available Synapse dataset. Code is available at: <https://github.com/duttapallabi2907/UVixLSTM>

1 Introduction

AI-driven medical image segmentation is one of the pivotal cornerstones of modern-day healthcare, providing essential information for diagnosing, planning treatment, and monitoring patients. Volumetric medical image data within a specific Volume of Interest (VOI), offers a comprehensive depiction of various pathologies and anatomical structures in terms of their volume, shape, and/or density [1]. This involves examining the spatial relationship between Regions of Interest (ROIs) across numerous slices of the volumetric data. Nevertheless, there are various challenges in accurately defining target regions from complex medical data with multiple dimensions. The challenges stem from the complex characteristics of multi-dimensional medical data, which necessitate achieving a high degree of accuracy and precision in the output.

Deep learning [2] is widely used for automated medical image segmentation primarily because of its ability to extract vital features from input images with minimal human involvement and can generalize well to new, unseen samples [3]. The U -Net architecture [4], consisting of symmetric encoder-decoder structures with CNNs, played a crucial role in revolutionizing the extensive use of deep learning in medical image segmentation. Hierarchical modeling of complex high-level patterns from low-level features and integration of fine-grained spatial information with coarser abstract features are the factors attributing to the success of U -Net. Expanding on the accomplishments of U -Net,

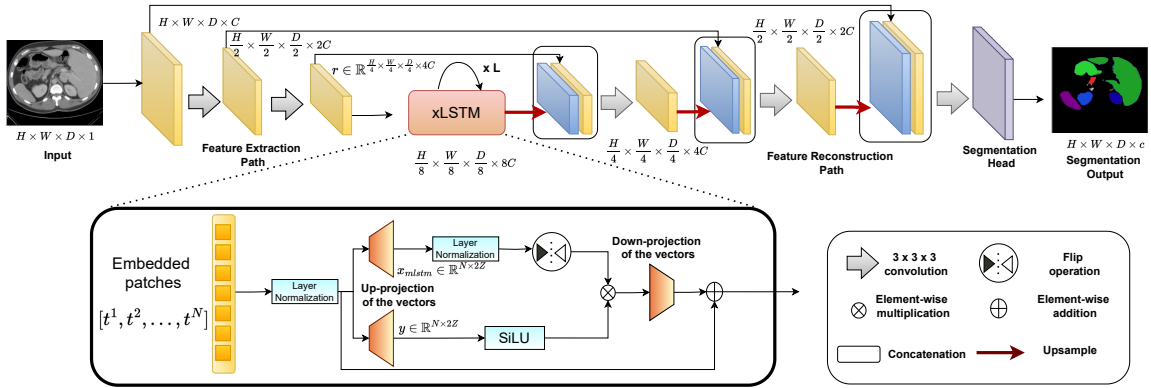


Figure 1: Architectural framework of *UVixLSTM* depicting the input processed by stacked layers of CNNs and Vision-xLSTM blocks. The intermediate feature representation from the feature extraction path is upsampled through the feature reconstruction path to obtain the final segmentation output.

various well-known architectures have been developed, such as *U-Net++* [5], *V-Net* [6], *Attention U-Net* [7], and *U-Net 3+* [8]. Each of these architectures introduces distinct modifications to improve performance and tackle specific difficulties in medical image segmentation.

In the quest for more efficient architectures, hybrid combinations of CNNs and Transformers are explored to combine their benefits to create a robust representation of target structures. Transformers overcome a significant drawback of CNNs through their self-attention mechanism, enabling them to effectively capture global relationships. In contrast, CNNs mostly concentrate on local patterns. *TransUNet* [9] pioneers the study of the impact of such a hybrid structure in medical image segmentation. It models the global structural dependencies in the intermediate feature volumes produced from CNN layers using the self-attention mechanism of Transformers [10]. This framework was further adopted into multiple segmentation tasks in the medical domain with necessary modifications [11], [12] and [13]. Some other well-known hybrid CNN-Transformer architectures in this domain include *UNETR* [14], *Swin UNETR* [15], *TransAttUNET* [16] and *DS-TransUNet* [17].

Self-attention mechanism, the driving force of Transformers, suffers from the curse of quadratic complexity leading to huge computational complexity and memory usage. This makes the applicability of Transformers limited in resource-restricted environments. Extended Long-Short Term Memory (xLSTM) [18] have recently emerged as strong contenders to the Transformers in sequence modeling. They address the key limitations of Transformers with their linear computational complexity ($\mathcal{O}(n)$) and constant memory complexity ($\mathcal{O}(1)$) w.r.t the length of input sequences. *Vision-xLSTM*¹ [19] pioneers the application of xLSTMs to computer vision tasks.

Apart from developing deep algorithms that exhibit efficient performance at the task at hand, developing algorithms that are efficient in terms of their computing resource consumption is also an essential requirement. It ensures the scalability of AI-driven algorithms in real-world scenarios. In clinical scenarios with limited computing resources, it is important to have models that can accurately delineate target structures from volumetric medical data while limiting the amount of computational power and memory required. It is essential for guaranteeing cost-efficient healthcare solutions.

In this research, to the best of our knowledge, we develop the first model, *UVixLSTM* that integrates CNNs with Vision-xLSTMs based on the popular *U*-shaped framework [20], [21], [22], [23] for medical image segmentation tasks. CNNs initially capture the fine-grained textural information and local patterns corresponding to the target anatomical structures from the volumetric input data. The Vision-xLSTM blocks encode the global context in a computationally effective manner. Experimental results obtained by deploying the model on a publicly available multi-organ segmentation dataset *Synapse* [24] illustrates the efficiency of our proposed work in terms of performance as well as computing resources utilization.

2 Methodology

Fig. 1 illustrates the structural framework of our proposed *UVixLSTM*. The network architecture resembles an hourglass structure, characterized by feature extraction and reconstruction pathways. The feature extraction arm consists of

¹<https://github.com/nx-ai/vision-lstm>

hybrid CNN-Vision-xLSTM blocks that progressively reduce the size of the feature volumes to obtain a high-level abstract representation of the image. The reconstruction path gradually builds the high-dimensional segmentation output using the low-dimensional contextual representation from the preceding feature extraction path. The output of each convolution block in the feature extraction path is directed to its corresponding counterpart at the same level of the feature reconstruction path, through skip connections, to facilitate the integration of feature maps originating at various levels of abstraction. This ensures judicious combination of the finer textural details from earlier convolutional levels with the coarser semantic information of the deeper levels; thereby, resulting in enhanced context-sensitive predictions. The subsequent text within this section is further divided into three parts *viz.* CNNs for high-level feature learning, Vision-xLSTM for global dependencies and the feature reconstruction path to present the key components of our architecture in detail.

2.1 Feature Extraction Path

2.1.1 CNNs for High-Level Feature Learning

The volumetric input image; $I \in \mathbb{R}^{H \times W \times D \times C}$ is subjected to a series of convolution layers that hierarchically construct an intermediate abstract and high-level representation of the image denoted by $r \in \mathbb{R}^{\frac{H}{4} \times \frac{W}{4} \times \frac{D}{4} \times 4C}$. Here, H , W and D represent the height, width and depth of the intermediate feature volume with C corresponding to the number of channels.

Eventually, r is divided into non-overlapping patches, each with a dimension of $P \times P \times P$. This is followed by flattening the patches into 1D vectors to yield tokenized representation $t \in \mathbb{R}^{N \times (P^3 \frac{C}{4})}$. Here $N = (\frac{H}{4} \times \frac{W}{4} \times \frac{D}{4}) / P^3$ denotes the number of patches and $P^3 \frac{C}{4}$ is the dimension of each flattened patch. The flattened patches are projected to a Z -dimensional embedding space with learnable positional embeddings added to preserve the spatial location information. Mathematically, it is expressed as

$$p = [t^1 \mathbf{K}; t^2 \mathbf{K}; \dots; t^N \mathbf{K}] + K_{pos} \quad (1)$$

$\mathbf{K} \in \mathbb{R}^{(P^3 \frac{C}{4} \times Z)}$ is the projection matrix and $\mathbf{K}_{pos} \in \mathbb{R}^{N \times Z}$ is the position embedding matrix.

2.1.2 Vision-xLSTM for Global Dependencies

The projected patches are subjected to a stack of Vision-xLSTM (ViL) [19] blocks. The structure comprises alternating mLSTM blocks with even-numbered blocks processing patch tokens from the top left to the bottom right and odd-numbered blocks from the bottom right to the top left. This bi-directional processing enables ViL blocks to capture robust global dependencies in the input.

The flattened patches after being normalized are projected to an embedding space, increasing their dimension by a factor of 2. These expanded embeddings are divided into two paths: $x_{mlstm} \in \mathbb{R}^{N \times 2Z}$ and $y \in \mathbb{R}^{N \times 2Z}$. x_{mlstm} undergoes a 1D causal convolution operation with the SiLU activation function applied to it. The intermediate result ($\mathbf{X} \in \mathbb{R}^{N \times 2Z}$) is then mapped onto query (q), key (k) and value (v) vectors, which are similar to the vectors used in the Transformer architecture. These vectors are further carried forward to mLSTM cell. The mLSTM sublayer comprises n parallel attention heads, each equipped with a matrix memory cell. The generation of query, value and keys is mathematically expressed as:

$$\mathbf{Q} = \mathbf{XW}_Q^T, \quad \mathbf{K} = \mathbf{XW}_K^T, \quad \mathbf{V} = \mathbf{XW}_V^T \quad (2)$$

where $\mathbf{Q} \in \mathbb{R}^{N \times d}$, $\mathbf{K} \in \mathbb{R}^{N \times d}$, $\mathbf{V} \in \mathbb{R}^{N \times d}$ are the query, key and value matrices, and $W_Q \in \mathbb{R}^{2Z \times d}$, $W_K \in \mathbb{R}^{2Z \times d}$, $W_V \in \mathbb{R}^{2Z \times d}$ are the learnable weight matrices to generate the query, key, and value for each head. Here d is the target dimension for the queries, keys, and values.

At first, input and forget gate pre-activations, $\tilde{i} \in \mathbb{R}^{N \times d_h}$ and $\tilde{f} \in N \times d_h$ respectively, are calculated by linearly projecting the concatenated \mathbf{Q} , \mathbf{K} and \mathbf{V} matrices as expressed below mathematically:

$$\tilde{i} = \mathbf{W}^I[\mathbf{Q}, \mathbf{K}, \mathbf{V}] + \mathbf{B} \quad (3)$$

$$\tilde{f} = \mathbf{W}^F[\mathbf{Q}, \mathbf{K}, \mathbf{V}] + \mathbf{B} \quad (4)$$

Here, $\mathbf{B} \in \mathbb{R}^{N \times d_h}$ is the bias matrix. The pre-activations are further used to derive the gate decay matrix $\mathbf{D} \in N \times d_h$ based on the following equation:

$$\mathbf{D} = \tilde{i} \oplus l\sigma(\tilde{f}) \quad (5)$$

Here $l\sigma$ denotes the log-sigmoid activation function. The decay matrix \mathbf{D} is further stabilized to ensure that subsequent exponentiation of \mathbf{D} produces stable output. The final gate decay matrix output $\hat{\mathbf{D}} \in N \times d_h$ is expressed as:

$$\hat{\mathbf{D}} = \exp(\mathbf{D}) \quad (6)$$

Here \exp is the exponentiation operation. The \mathbf{Q} and \mathbf{K} vectors undergo dot product multiplication to get the attention scores $\mathbf{S} \in \mathbb{R}^{N \times N}$, analogous to the self-attention mechanism in Transformers. A causal mask $\mathbf{M} \in \mathbb{R}^{N \times N}$ guarantees that attention is directed exclusively from the previous patch to the current patch. It is mathematically expressed as:

$$\mathbf{S} = \text{Softmax}\left(\frac{\mathbf{Q}\mathbf{K}^\top}{\sqrt{d}} + \mathbf{M}\right) \quad (7)$$

The attention score matrix is element-wise multiplied with $\hat{\mathbf{D}}$ to get the combination matrix $\mathbf{C} \in \mathbb{R}^{N \times d_h}$.

$$\mathbf{C} = \mathbf{S}^\top \hat{\mathbf{D}} \quad (8)$$

Finally, we obtain the updated cell state \tilde{h}_t as:

$$\tilde{h}_t = \mathbf{C} \otimes \mathbf{V} \quad (9)$$

Subsequently, the embedding y generated from the second path is multiplied with \tilde{h}_t followed by a down-projection operation to project the final output o to Z -dimensional embedding space. It is mathematically expressed as follows:

$$o = \mathbf{W}^{\mathbf{D}} (y \otimes \tilde{h}_t) \quad (10)$$

Here $\mathbf{W}^{\mathbf{D}} \in \mathbb{R}^{2Z \times Z}$ is the projection matrix.

2.2 Feature Reconstruction Path

At every level l in the feature reconstruction path, a trilinear upsampling operation τ is employed to increase the spatial dimension of the feature maps obtained from the preceding level $l + 1$. This helps align the spatial dimensions of the feature maps with those received from the corresponding level l from the feature extraction path.

$$\mathbf{U}_l = \tau(\mathbf{V}_{l+1}) \quad (11)$$

where \mathbf{U}_l is the upsampled feature map at level l and \mathbf{V}_{l+1} is the output volume from level $l + 1$.

The upsampled feature map \mathbf{U}_l is then concatenated with the feature map from the corresponding level l of the feature extraction path, denoted as \mathbf{F}_l :

$$\mathbf{C}_l = \text{Concat}(\mathbf{U}_l, \mathbf{F}_l) \quad (12)$$

where \mathbf{C}_l is the concatenated feature volume at level l .

The concatenated feature volume \mathbf{C}_l is then subjected to a convolution operation to yield the output volume \mathbf{V}_l of level l in the feature reconstruction path:

$$\mathbf{V}_l = \text{Conv}(\mathbf{C}_l) \quad (13)$$

3 Implementation and Experimental Details

3.1 Loss Function and Performance Metrics

A loss function combination of Dice (\mathcal{L}_{dice}) and Categorical-Cross Entropy [25] (\mathcal{L}_{cce}) was used to train our proposed network. Mathematically \mathcal{L}_{dice} and \mathcal{L}_{cce} is expressed as:

$$\mathcal{L}_{dice} = \gamma - \sum_{\gamma=1}^c \left(\frac{2 \sum_{i=1}^T \hat{z}_{\gamma,i} z_{\gamma,i} + \mu}{\sum_{i=1}^T \hat{z}_{\gamma,i} + z_{\gamma,i} + \mu} \right), \quad (14)$$

$$\mathcal{L}_{cce} = -\frac{1}{T} \sum_{i=1}^T \sum_{\gamma=1}^c z_{\gamma,i} \log(\hat{z}_{\gamma,i}). \quad (15)$$

Table 1: Comparison of different variants of *UVixLSTM* with increasing number of Vision-xLSTM blocks. The best results are highlighted in **bold**.

Number of Vision-xLSTM blocks	DSC	IoU	HD95
x 6	0.8318	0.7323	4.8
x 12	0.8289	0.7286	8.57
x 18	0.8201	0.7189	4.34
x 24	0.8299	0.728	19.05

Table 2: Comparison with the state-of-the-art models on the multi-organ segmentation (Synapse) dataset. The best results are highlighted in **bold**.

Model	Dice										IoU Mean	HD95 Mean
	Spleen	Right kidney	Left kidney	Gall Bladder	Liver	Pancreas	Stomach	Right Adrenal	Left Adrenal	Mean		
UNet	0.9112	0.9007	0.9181	0.5645	0.9572	0.6967	0.78	0.616	0.5872	0.7702	0.6667	38.83
V-Net	0.8874	0.9251	0.9244	0.5858	0.9487	0.7511	0.7953	0.6004	0.4497	0.7631	0.6537	25.29
UNet++	0.9118	0.9196	0.8905	0.6921	0.9524	0.7536	0.7869	0.5245	0.1032	0.7261	0.6254	55.27
Attention U-Net	0.9109	0.877	0.872	0.5835	0.9585	0.5566	0.7846	0.5991	0.5398	0.7424	0.6262	51.61
UNet + EfficientNet-b0	0.8541	0.8919	0.8804	0.637	0.9077	0.5018	0.7097	0.6048	0.5195	0.723	0.6056	67.47
UNet + EfficientNet-b1	0.7414	0.8059	0.8256	0.55	0.9019	0.5416	0.616	0.525	0.5035	0.6679	0.5539	75.85
UNet 3+	0.8736	0.9229	0.8584	0.6659	0.9383	0.6823	0.7259	0.5657	0.4764	0.7455	0.6254	54.43
SwinUNet	0.9482	0.93	0.9245	0.7617	0.9622	0.8046	0.8059	0.689	0.6159	0.8269	0.7261	13.99
UNETR	0.8951	0.9055	0.895	0.5274	0.9461	0.6668	0.7847	0.5268	0.4978	0.7384	0.6284	26.94
TransUNET	0.852	0.8828	0.785	0.7608	0.587	0.7218	0.8773	0.5876	0.4672	0.7246	0.6679	36.81
TransAttUNET	0.9045	0.8761	0.916	0.4958	0.9408	0.5997	0.6682	0.6559	0.5948	0.7391	0.658	15.82
DiffUNET	0.8633	0.8042	0.8454	0.5946	0.9438	0.6469	0.66	0.5999	0.5046	0.7181	0.6306	27.57
DS-TransUNET	0.4965	0.6113	0.5252	0.5397	0.679	0.5295	0.5857	0.5745	0.5266	0.5631	0.4644	14.79
<i>UVixLSTM</i>	0.95	0.9371	0.9366	0.8104	0.9635	0.7878	0.8304	0.6709	0.6458	0.8318	0.7286	4.8

Here, c represents the total number of classes that need to be predicted in the input volume. $\hat{z}_{\gamma,i}$ and $z_{\gamma,i}$ represent the predicted and ground truth values (respectively) for the i^{th} voxel for class γ . T denotes the total number of voxels in the input, and μ is the additive smoothing parameter used to avoid division-by-zero errors.

The composite loss function \mathcal{L} is expressed as:

$$\mathcal{L}(\{\hat{\rho}, \rho\}; \Gamma) = \mathcal{L}_{dice}(\{\hat{\rho}, \rho\}, \Gamma) + \mathcal{L}_{cce}(\{\hat{\rho}, \rho\}, \Gamma), \quad (16)$$

Γ denotes the model parameters and $\hat{\rho}$ and ρ , symbolize the predicted segmentation map and the ground truth, respectively.

The Dice Score Coefficient (*DSC*), Intersection-Over-Union (*IoU*), and 95% Hausdorff Distance (*HD95*) are the performance metrics employed for evaluating the segmentation output.

3.2 Datasets

The Synapse dataset [24] comprises 30 CT volumes with sizes varying from $512 \times 512 \times 85$ to $512 \times 512 \times 198$. The CT volumes are annotated manually by domain experts to highlight the different abdominal organs. The model is trained to segment nine distinct organs of the abdominal cavity *viz.* spleen, left kidney, right kidney, liver, gall bladder, pancreas, stomach, right adrenal gland, and left adrenal gland. The spleen, liver, and stomach are classified as larger organs, whereas the kidneys, gall bladder, pancreas, and adrenal glands are smaller in size.

The CT volumes were partitioned into train and test set, with 80% used for training and the remaining 20% used for testing to evaluate the models' generalization performance. The voxel intensities were restricted to a range of -170 HU to 250 HU in order to improve the visibility of anatomical features and reduce noise. Subsequently, intensity normalization was conducted to adjust the values so that they fall within the range of [0,1]. Data augmentation was effective in expanding the size of the training dataset. The techniques involved in this process encompass flipping the data across the height, width, and depth axes, performing random rotations on the data, and introducing random variations in intensity values. This helped to mitigate the difficulty caused by the restricted accessibility of datasets for training deep learning models.

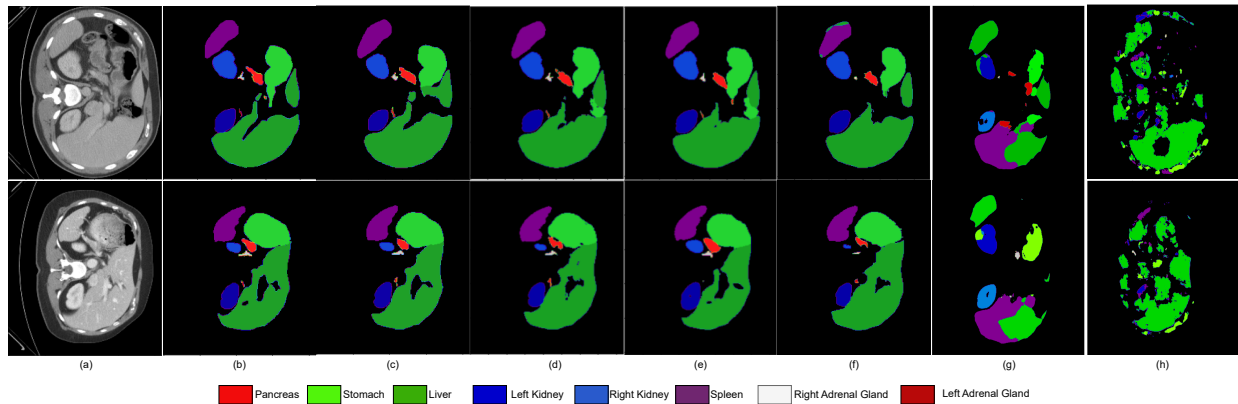


Figure 2: Comparison of the performance of *UVixLSTM* and other baseline architectures on the *Synapse* dataset through sample segmentation maps. (a) The input CT image, (b) the corresponding ground truth and (c) the corresponding output from the *UVixLSTM*. This includes (d) Swin UNETR, (e) UNETR, (f) V-Net, (g) TransAttUNet, and (h) DS-TransUNet.

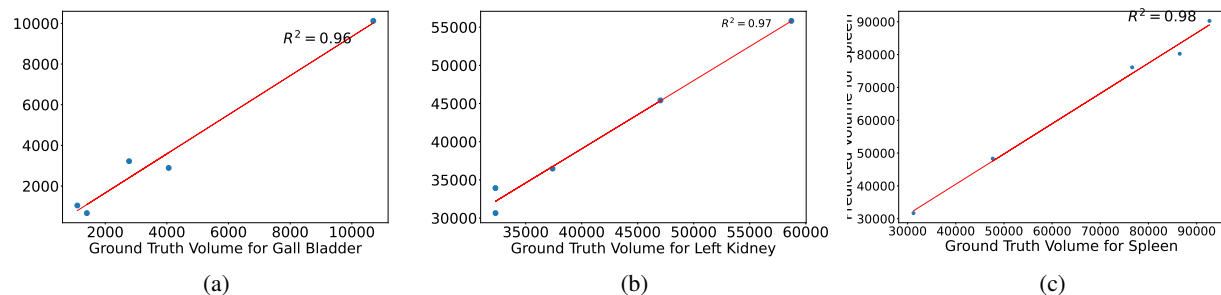


Figure 3: Scatter plots comparing the ground truth volumes and predicted volumes of (a) Gall Bladder (b) Left Kidney and (c) Spleen. Each data point represents an individual instance from the dataset.

3.3 Results

Table 1 tabulates the ablation study results demonstrating the impact of different numbers of Vision-xLSTM blocks. The average *DSC*, *HD95* and *IoU* scores are reported for the different organs. The best *DSC* and *IoU* values are obtained with the lowest number of Vision-xLSTM blocks. This implies with lower computational and memory requirements, *UVixLSTM* can achieve efficient with significant advantage of deployment in resource-constrained environment.

The performance of the *UVixLSTM* model was evaluated against state-of-the-art (SOTA) algorithms in the literature, such as *U-Net* [4], *V-Net* [6], *U-Net++* [5], *Attention U-Net* [7], *U-Net 3+* [8], *U-Net* with EfficientNet-b0 [26] backbone, *U-Net* with EfficientNet-b1 [26] backbone, Swin UNETR [15], TransUNet [9], UNETR [14], DS-TransUNet [17], DiffUNet [27] and TransAttUNet [16] in terms of the metrics *DSC*, *IoU*, *HD95*. Table 2 presents a comprehensive breakdown of the different organs in the context of *DSC*. The average outcomes for *HD95* and *IoU* are provided for all nine abdominal organs. *UVixLSTM* outperforms other SOTA methods with respect to average *DSC*, *IoU* and *HD95* scores of 83.18%, 72.86% and 4.8 respectively. Our proposed method demonstrated superior performance in generating the highest *DSC* values for the segmentation of larger organs (like the spleen, liver) as well as smaller organs (like the kidneys, pancreas, gall bladder and left adrenal gland). The model’s performance remained stable despite the reduction in organ size, as indicated by the consistent high *DSC* scores observed for small and large organs. This illustrates the capacity of our model to efficiently utilize acquired knowledge on anatomical structures with varying shapes and sizes. It is highly efficient in precisely identifying and defining target areas that possess unique structures.

Fig. 2 illustrates the sample segmentation output of *UVixLSTM* and other architectures like Swin-UNETR, UNETR, V-Net, TransAttUNet and DS-TransUNet. In the sample maps it is evident that the *UVixLSTM* model shows a significantly higher level of similarity to the ground truth compared to the maps produced by other baseline models. The results from Swin UNETR and UNETR models show *FP* regions corresponding to the stomach in the first row of Figure 2 (d) and (e). The outcomes from the V-Net in the uppermost row of Fig. 2 (f) demonstrate that the pixels associated with the boundary areas of the spleen were inaccurately classified. Furthermore, it demonstrates a lack of precision in identifying

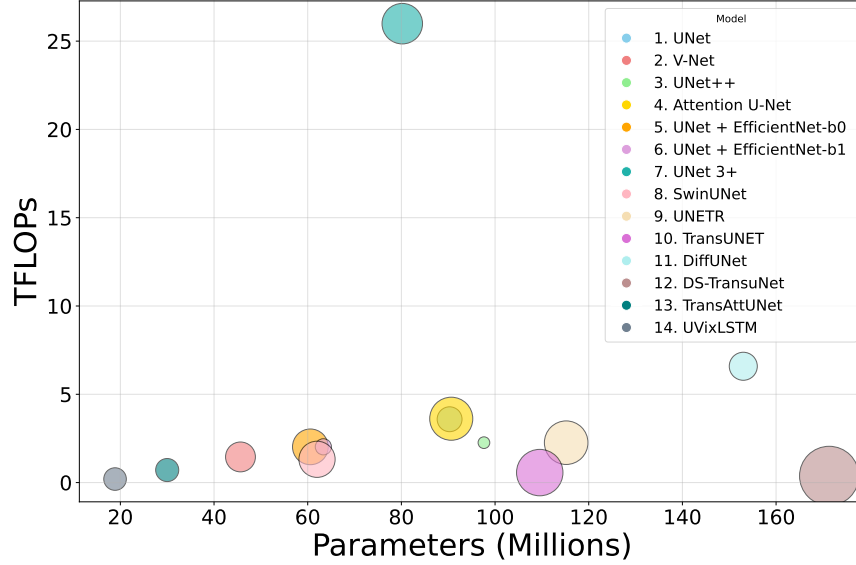


Figure 4: Comparison between models w.r.t number of parameters (in millions), TFLOPs and memory size (in MB). Bubble size is indicative of the model size.

the anatomical regions linked to the left adrenal gland, as well as insufficient division of the right adrenal gland. The segmentation maps obtained from TransAttUNet and DS-TransUNet exhibits their limited capacity in learning complex representations corresponding to the multiple organs with varying shapes and sizes.

Fig. 3 shows the regression coefficient (R^2) [28], as well as a fitted regression line that represents the predicted volumes by *UVixLSTM* compared to the actual volumes for gall bladder, left kidney and spleen. The high coefficient of determination (R-squared) value indicates a robust linear relationship between the variables, suggesting that the predictions remain consistent across various sample points.

Fig. 4 provides a graphical analysis of the parameter count, Tera Floating point OPERations (TFLOPs) and memory size on disk of *UVixLSTM* compared to the other baseline architectures under consideration. The analysis shows that *UVixLSTM* has the lowest number of parameters and TFLOPs (floating point operations per second) compared to the other algorithms. This confirms our assertion about the superior computational efficiency of the proposed model. Thereby, it has the potential to be deployed in resource-constrained environments.

4 Discussion

The superiority of our model can be ascribed to various factors. The incorporation of CNNs with Vision-xLSTM allows the model to effectively capture both local and global contextual information, which is essential for achieving precise segmentation. Furthermore, the utilization of Vision-xLSTM enhances the efficiency of the model in terms of the overall number of parameters and FLOPs when compared to other hybrid CNN-Transformer methods. This has substantial implication in clinical practices by increasing the accessibility of our model in settings with limited resources. This can potentially result into expedited and effective identification of medical conditions, strategizing for treatment, and providing guidance during surgical procedures.

This study pioneers in the integration of CNNs with Vision-xLSTMs for developing efficient framework for medical image segmentation task. In our future research, we aim to broaden the range of this study by utilizing the model in different medical image segmentation tasks. This will comprehensively assess its ability to generalize and uncover any possible limitations.

5 Conclusions

This paper introduces the first integration of CNNs with Vision-xLSTMs for medical image segmentation, utilizing the widely used *U*-shaped framework. The CNNs acquire intricate spatial and textural information from the input image. On the other hand, the Vision-xLSTMs capture both global and temporal relationships inside the patches

derived from the feature volume produced by CNNs, thereby learning a robust representation for the target structures. The experimental results suggest that our proposed work *UVixLSTM* surpasses other fully convolutional and hybrid CNN-Transformer architecture in terms of performance and resource efficiency. This makes our work a potential candidate for getting deployed in resource-constrained clinical settings.

Acknowledgement

This work was supported by the J. C. Bose National Fellowship, grant no. JCB/2020/000033 of S. Mitra.

References

- [1] G. H. Choi, J. Yun, and *et al.*, “Development of machine learning-based clinical decision support system for hepatocellular carcinoma,” *Scientific Reports*, vol. 10, p. 14855, 2020.
- [2] Y. LeCun, Y. Bengio, and *et al.*, “Deep learning,” *Nature*, vol. 521, pp. 436-444, 2015.
- [3] X. Chen, X. Wang, and *et al.*, “Recent advances and clinical applications of deep learning in medical image analysis,” *Medical Image Analysis*, vol. 79, p. 102444, 2022.
- [4] O. Ronneberger, P. Fischer, and *et al.*, “U-Net: Convolutional networks for biomedical image segmentation,” in *Proceedings of the International Conference on Medical Image Computing and Computer Assisted Intervention (MICCAI)*, pp. 234-241, Springer, 2015.
- [5] Z. Zhou, R. Siddiquee, and *et al.*, “U-Net++: A nested U-Net architecture for medical image segmentation,” in *Deep Learning in Medical Image Analysis and Multimodal Learning for Clinical Decision Support*, pp. 3-11, Springer, 2018.
- [6] F. Milletari, N. Navab, and *et al.*, “V-Net: Fully convolutional neural networks for volumetric medical image segmentation,” in *Proceedings of Fourth International Conference on 3D vision (3DV)*, pp. 565-571, IEEE, 2016.
- [7] O. Oktay, J. Schlemper, and *et al.*, “Attention U-Net: Learning where to look for the pancreas,” in *Proceedings of the Medical Imaging with Deep Learning*, pp. 1–10, 2018.
- [8] H. Huang, L. Lin, and *et al.*, “U-Net 3+: A full-scale connected U-Net for medical image segmentation,” in *Proceedings of IEEE International Conference on Acoustics, Speech and Signal Processing (ICASSP)*, pp. 1055–1059, IEEE, 2020.
- [9] J. Chen, Y. Lu, and *et al.*, “TransUNet: Transformers make strong encoders for medical image segmentation,” *arXiv preprint arXiv:2102.04306*, 2021.
- [10] A. Vaswani, N. Shazeer, and *et al.*, “Attention is all you need,” *Advances in Neural Information Processing Systems*, vol. 30, 2017.
- [11] J. Cheng, J. Liu, and *et al.*, “A fully automated multimodal MRI-based multi-task learning for glioma segmentation and IDH genotyping,” *IEEE Transactions on Medical Imaging*, vol. 41, pp. 1520–1532, 2022.
- [12] R. Pemmaraju, D. Y. Song, and *et al.*, “Cascaded neural network segmentation pipeline for automated delineation of prostate and organs at risk in male pelvic CT,” in *Proceedings of Medical Imaging 2023: Image Processing*, vol. 12464, pp. 311–318, SPIE, 2023.
- [13] B. Wang, F. Wang, and *et al.*, “Multiscale TransUNet++: Dense hybrid U-Net with transformer for medical image segmentation,” *Signal, Image and Video Processing*, vol. 16, pp. 1607–1614, 2022.
- [14] A. Hatamizadeh, Y. Tang, and *et al.*, “UNETR: Transformers for 3D medical image segmentation,” in *Proceedings of the IEEE/CVF Winter Conference on Applications of Computer Vision*, pp. 574–584, 2022.
- [15] A. Hatamizadeh, V. Nath, and *et al.*, “Swin UNETR: Swin transformers for semantic segmentation of brain tumors in MRI images,” in *Proceeding of International MICCAI Brainlesion Workshop*, pp. 272–284, Springer, 2021.
- [16] B. Chen, Y. Liu, and *et al.*, “TransAttUNet: Multi-level attention-guided U-Net with transformer for medical image segmentation,” *IEEE Transactions on Emerging Topics in Computational Intelligence*, 2023.
- [17] A. Lin, B. Chen, and *et al.*, “DS-TransUNet: Dual swin transformer U-Net for medical image segmentation,” *IEEE Transactions on Instrumentation and Measurement*, vol. 71, pp. 1–15, 2022.
- [18] M. Beck, K. Pöppel, and *et al.*, “xLSTM: Extended Long Short-Term Memory,” *arXiv preprint arXiv:2405.04517*, 2024.
- [19] B. Alkin, M. Beck, and *et al.*, “Vision-LSTM: xLSTM as generic vision backbone,” *arXiv preprint arXiv:2406.04303*, 2024.

- [20] M. M. Rahman, S. Shokouhmand, and *et al.*, “MIST: Medical Image Segmentation Transformer with Convolutional Attention Mixing (CAM) decoder,” in *Proceedings of the IEEE/CVF Winter Conference on Applications of Computer Vision*, pp. 404–413, 2024.
- [21] X. Yan, H. Tang, and *et al.*, “After-UNet: Axial fusion transformer unet for medical image segmentation,” in *Proceedings of the IEEE/CVF Winter Conference on Applications of Computer Vision*, pp. 3971–3981, 2022.
- [22] P. Dutta and S. Mitra, “Efficient global-context driven volumetric segmentation of abdominal images,” in *2023 IEEE International Conference on Bioinformatics and Biomedicine (BIBM)*, pp. 1880–1885, 2023.
- [23] P. Dutta and S. Mitra, “Full-scale deeply supervised attention network for segmenting COVID-19 lesions,” in *Proceedings of 20th International Symposium on Biomedical Imaging (ISBI)*, IEEE, 2023.
- [24] B. Landman, Z. Xu, and *et al.*, “MICCAI multi-atlas labeling beyond the cranial vault—workshop and challenge,” in *Proceedings of MICCAI Multi-Atlas Labeling beyond Cranial Vault—Workshop Challenge*, p. 12, 2015.
- [25] S. A. Taghanaki, Y. Zheng, and *et al.*, “Combo loss: Handling input and output imbalance in multi-organ segmentation,” *Computerized Medical Imaging and Graphics*, vol. 75, pp. 24–33, 2019.
- [26] M. Tan and Q. Le, “EfficientNet: Rethinking model scaling for convolutional neural networks,” in *Proceedings of International Conference on Machine Learning (ICML)*, pp. 6105–6114, PMLR, 2019.
- [27] Z. Xing, L. Wan, and *et al.*, “Diff-UNet: A diffusion embedded network for volumetric segmentation,” *arXiv preprint arXiv:2303.10326*, 2023.
- [28] A. J. Hughes and D. E. Grawoig, *Statistics: A Foundation For Analysis*. Addison Wesley Publishing Company, 1971.